



OBSERVATIONAL CONSTRAINTS ON THE ORBIT AND LOCATION OF PLANET NINE IN THE OUTER SOLAR SYSTEM

MICHAEL E. BROWN AND KONSTANTIN BATYGIN

Division of Geological and Planetary Sciences, California Institute of Technology, Pasadena, CA 91125, USA;

mbrown@caltech.edu, kbatygin@gps.caltech.edu

Received 2016 March 17; revised 2016 May 19; accepted 2016 May 24; published 2016 June 17

ABSTRACT

We use an extensive suite of numerical simulations to constrain the mass and orbit of Planet Nine, the recently proposed perturber in a distant eccentric orbit in the outer solar system. We compare our simulations to the observed population of aligned eccentric high semimajor axis Kuiper belt objects (KBOs) and determine which simulation parameters are statistically compatible with the observations. We find that only a narrow range of orbital elements can reproduce the observations. In particular, the combination of semimajor axis, eccentricity, and mass of Planet Nine strongly dictates the semimajor axis range of the orbital confinement of the distant eccentric KBOs. Allowed orbits, which confine KBOs with semimajor axis beyond 380 au, have perihelia roughly between 150 and 350 au, semimajor axes between 380 and 980 au, and masses between 5 and 20 Earth masses. Orbitally confined objects also generally have orbital planes similar to that of the planet, suggesting that the planet is inclined approximately 30° to the ecliptic. We compare the allowed orbital positions and estimated brightness of Planet Nine to previous and ongoing surveys which would be sensitive to the planet's detection and use these surveys to rule out approximately two-thirds of the planet's orbit. Planet Nine is likely near aphelion with an approximate brightness of $22 < V < 25$. At opposition, its motion, mainly due to parallax, can easily be detected within 24 hours.

Key words: celestial mechanics – Kuiper belt: general – planets and satellites: detection

1. INTRODUCTION

Since the time of the discovery of Sedna, it has been clear that a large perturbing mass either is or was present in the outer solar system at some time (Brown et al. 2004). With a perihelion distance of 76 au, Sedna is essentially immune to direct interactions with the known planets; thus, unlike all other Kuiper belt object (KBO) orbits, it cannot have been placed onto its orbit by perturbation from any of the known planets. Proposals for the perturber required to have created Sedna's orbit have included sibling stars in the Sun's birth cluster (Brown et al. 2004; Brasser et al. 2006; Dukes & Krumholz 2012), a single passing star (Kenyon & Bromley 2004; Morbidelli & Levison 2004; Rickman et al. 2004) as well as a small former or extant planet in the outer solar system (Brown et al. 2004; Gladman & Chan 2006; Gomes et al. 2006). Progress on understanding the cause of Sedna's perturbed orbit, however, was not possible because of a lack of additional high perihelion objects.

With the discovery of 2010 GB174 (Chen et al. 2013) and 2012 VP113 (Trujillo & Sheppard 2014)—the second and third high-perihelion Sedna-like objects—additional patterns began to emerge. Most importantly, Batygin & Brown (2016) point out that all well-determined orbits of KBOs beyond Neptune with semimajor axis, a , larger than 227 au approach perihelion within 94° of longitude of each other. Moreover, these objects also share very nearly the same orbital plane, which is tilted an average of 22° to the ecliptic. The combined probability of these two occurrences happening simply due to chance is less than 0.01%. Importantly, of all KBOs with $a > 100$ au, the five with the largest perihelion distances are likewise confined to the same perihelion region and orbital plane.

Batygin & Brown (2016) show that a distant massive eccentric planet will cause clustering of the perihelion and orbital planes of distant KBOs in the manner observed, and,

additionally, will naturally lead to the creation of objects with high perihelion orbits like Sedna. Surprisingly, these clustered and high perihelion objects have orbits that are anti-aligned with the giant planet. That is, the clustered KBOs come to perihelion 180° away from the perihelion position of the planet. Despite chaotic evolution, the crossing orbits maintain long-term stability by residing on a interconnected web of phase-protected mean-motion resonances.

The distant eccentric perturber studied in Batygin & Brown (2016)—which we refer to as Planet Nine—modulates the perihelia of objects in the anti-aligned cluster and naturally creates objects like Sedna, in addition to the other high perihelion KBOs. Additionally, the existence of Planet Nine predicts a collection of high semimajor axis eccentric objects with inclinations essentially perpendicular to the rest of the solar system. Unexpectedly, this prediction is strongly supported by the collection of low perihelion Centaurs with perpendicular orbits whose origin had previously been mysterious (Gomes et al. 2015).

Here, we make detailed comparisons between dynamical simulations that include the effects of Planet Nine, and solar system observations, to place constraints on the orbit and mass of the distant planetary perturber. We then discuss observational constraints on the detection of this distant giant planet and future prospects for its discovery.

2. CONSTRAINTS ON MASS, SEMIMAJOR AXIS, AND ECCENTRICITY

The inclined orbits of the aligned KBOs (and thus, presumably, of the distant planet) render ecliptic-referenced orbital angles awkward to work in (particularly when we consider the Centaurs with perpendicular orbits later). Accordingly, we re-cast the three ecliptic-referenced parameters—argument of perihelion, longitude of ascending node, and

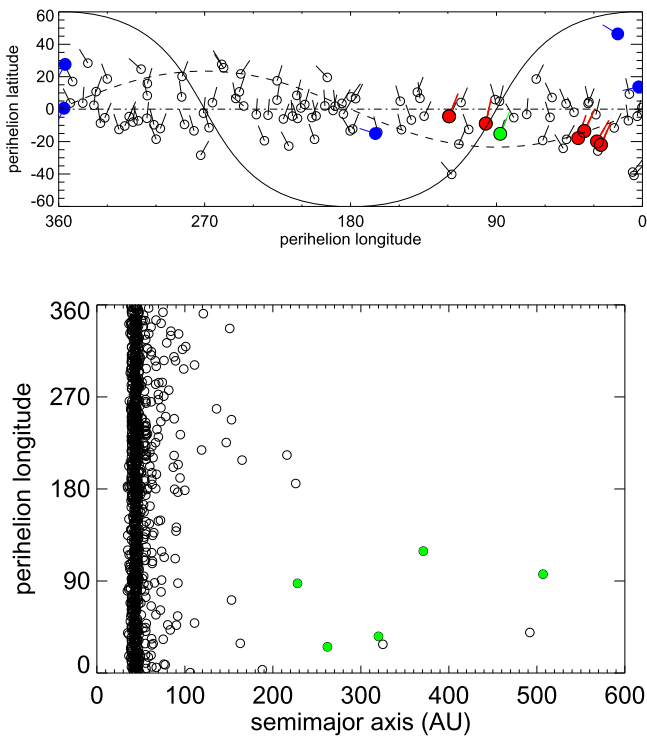


Figure 1. Orbital parameters of distant Kuiper belt objects. (a) The standard orbital parameters argument of perihelion, longitude of ascending node, and inclination can be transformed into non-standard, but more readily interpretable ecliptic longitude and latitude of the point where the object comes to perihelion and an angle that is a projection of the orbit’s pole position on the sky. In this representation, the collection of all objects with $q > 30$ and $a > 60$ au is shown. The six objects with the highest semimajor axis are highlighted in red. The KBO 2000 CR105, which has the seventh largest semimajor axis and has an elevated perihelion of 44 au, is shown in green. The blue points are all of the object with $a > 227$ au and $i > 50^\circ$. All of these objects are Centaurs with perihelia inside of 15 au. (b) A plot of the semimajor axis vs. the ecliptic longitude at which the object comes to perihelion for all KBOs with well-determined orbits and with $q > 30$ au shows that the seven KBOs with the largest semimajor axes are clustered within 94° of each other. The green points additionally highlight all objects with $a > 100$ au and $q > 42$ au, showing that these objects, too, are similarly clustered. The weaker potential clustering of objects $\sim 180^\circ$ away is also evident between 100 and 200 au.

inclination—into simple descriptions of orbit in absolute position on the sky: the ecliptic longitude of the point in the sky where the object is at perihelion (which we call the “perihelion longitude,” not to be confused with the standard orbital parameter called “longitude of perihelion” which, confusingly, does not actually measure the longitude of the perihelion except for zero inclination orbits), the latitude of the perihelion (“perihelion latitude”), and an angle that measures the projection of the orbit pole onto the plane of the sky (“pole angle” perhaps more easily pictured as the direction perpendicular to the motion of the object at perihelion).

Figure 1(a) shows the perihelion longitude and latitude as well as the pole angle for all objects with $q > 30$ and $a > 60$ au and well-determined orbits. The seven objects with $a > 227$ au are highlighted in red. The clustering in perihelion location as well as pole angle is clearly visible. In Figure 1(b), we plot the perihelion longitude of all well-constrained orbits in the Kuiper belt that have perihelia beyond the orbit of Neptune as a function of semimajor axis. The seven objects with $a > 227$ au cluster within 94° of perihelion longitude. Batygin & Brown (2016) showed that this clustering, when combined with the clustering in pole angle, was unexpected at the

99.993% confidence level. The clustering is consistent with that expected from a giant planet whose perihelion is located 180° in longitude away from the cluster, or an ecliptic longitude of $241^\circ \pm 15^\circ$. A closer examination of Figure 1(b) makes clear a possible additional unlikely phenomenon. While KBOs with semimajor axes out to 100 au appear randomly distributed in longitude, from 100 to 200 au, 13 objects are loosely clustered within 223° of each other. While this clustering is not as visually striking, the probability of such a loose clustering of 13 objects occurring in randomly distributed data is smaller than 5%. As will be seen, such a loose clustering of smaller semimajor axis objects can indeed be explained as a consequence of some orbital configurations of Planet Nine.

To understand how these observations constrain the mass and orbit of Planet Nine, we performed a suite of evolutionary numerical integrations. Specifically, we initialized a planar, axisymmetric disk consisting of 400 eccentric planetesimals that uniformly spanned semimajor axis and perihelion, q , distance ranges of $a = 150\text{--}550$ au and $q = 30\text{--}50$ au, respectively. The planetesimal population (treated as test particles) was evolved for 4 Gyr under the gravitational influence of the known giant planets, as well as Planet Nine.

Perturbations due to Planet Nine and Neptune were accounted for in a direct N-body fashion, while the secular effects of the remaining giant planets were modeled as a suitably enhanced quadrupolar field of the Sun. As shown in Batygin & Brown (2016), such a numerical setup successfully captures the relevant dynamical phenomena, at a substantially reduced computational cost.

In these integrations we varied the semimajor axis and eccentricity of Planet Nine from $a_9 = 200\text{--}2000$ au and $e_9 = 0.1\text{--}0.9$ in increments of $\Delta a_9 = 100$ au and $\Delta e_9 = 0.1$ (here, and subsequently, the nine subscript refers to the orbital parameters of Planet Nine, while unsubscripted orbital parameters refer to the test particles). The $a_9\text{--}e_9$ grids of synthetic scattered disks were constructed for Planet Nine masses of $m_9 = 0.1, 1, 10, 20,$ and $30M_\oplus$ (Earth masses), totaling a suite of 320 simulated systems. All calculations were performed using the `mercury6` N-body integration software package (Chambers 1999), employing the hybrid symplectic-Bulirsch-Stoer algorithm with a time step equal to one-tenth of Neptune’s orbital period.

We assess the success of each simulation with two simple metrics. First, we collect the orbital elements of all remnant objects at each 0.1 Myr output time step from 3 to 4 Gyr after the start of the simulation (in order to assure that the objects we are considering are stable over at least most of the age of the solar system), and we restrict ourselves to objects with instantaneous perihelion $q < 80$ au (to restrict ourselves to objects that are most likely to be observable). In this fashion we are examining stream functions of orbital elements that fit into an observable range of parameter space, rather than examining individual objects at a single time step. This approach is used in all subsequent discussions of simulations below. We then select 13 objects at random in the $a = [100, 200]$ au range and 7 objects at random in the $a = [227, 600]$ au range and calculate the smallest angles that can be used to confine the two populations. We perform this random selection 1000 times and calculate the joint probability that, like the real data, the 13 objects in $a = [100, 200]$ au range are confined within 223° and the 7 objects $a = [227\text{--}600]$ au range are confined within 94° . Additionally, we examine whether *any* objects exist

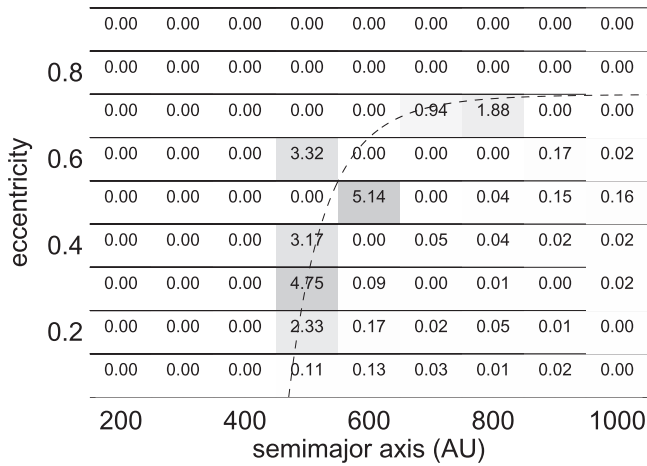


Figure 2. Only a limited set of simulated $10 M_e$ Planet Nine orbits provide an adequate fit to the known orbits of the distant KBOs. For each semimajor axis—eccentricity combination, we calculate the probability that 7 objects selected at random with $227 < a < 600$, $q < 80$ au and at times $t > 3$ Gyr are clustered within 94° of each other combined with the probability that 13 objects randomly selected with $100 < a < 200$ and $q < 80$ au. In addition we discard simulations with an unacceptably large probability of creating high perihelia in low semimajor axis objects. Acceptable simulations (with a probability of greater than 1%) occupy a narrow range of a_9 – e_9 space.

in the range $a = [200, 300]$ au, as many simulations remove all objects in this range. We assign these simulations a probability of zero. This probability calculation has the advantage that it is agnostic as to whether or not our observations of clustering are significant or even physically relevant. It simply calculates the probability that a given simulation could reproduce some of the apparent features of the real data, even if by chance.

The second metric we use to assess the success of the simulations relies on the observation of Batygin & Brown (2016) that a distant massive eccentric perturber will cause secular perturbations which lower the eccentricity and thus raise the perihelion of moderate semimajor axis objects at a wide range of perihelion latitudes. This effect increases strongly with increasing perturber eccentricity and with decreasing perturber semimajor axis. Of the 15 known KBOs with $100 < a < 220$ au and $q > 30$, zero have perihelion greater than 42 au (whereas 5 of the 7 objects with $a > 227$ au have such elevated perihelia). These simulations were not designed in such a way that simple assessment of the probability of such a distribution is straightforward. We approximate this probability by collecting all objects from time steps between 2 and 4 Gyr with $30 < q < 40$ au and $100 < a < 200$ au, randomly selecting 15 objects from this set, and calculating the product of the fraction of the time that each of these objects spends with $q < 42$ and $100 < a < 200$ au. These probabilities range from unity, when Planet Nine is distant or only mildly eccentric, to 10^{-12} for higher eccentricities and lower semimajor axes. Because these calculated probabilities are difficult to straightforwardly compare to the real data, we instead impose a simple threshold and assert that simulations with a 99% or higher probability of creating at least one high perihelion object in the $100 < a < 200$ au range are effectively ruled out. We assign their overall probability to zero.

Figures 2 and 3 show grids of probabilities for the 10 and 20 M_e simulations (the 0.1, 1, and 30 M_e simulations have no acceptable solutions). The probabilities should be taken as

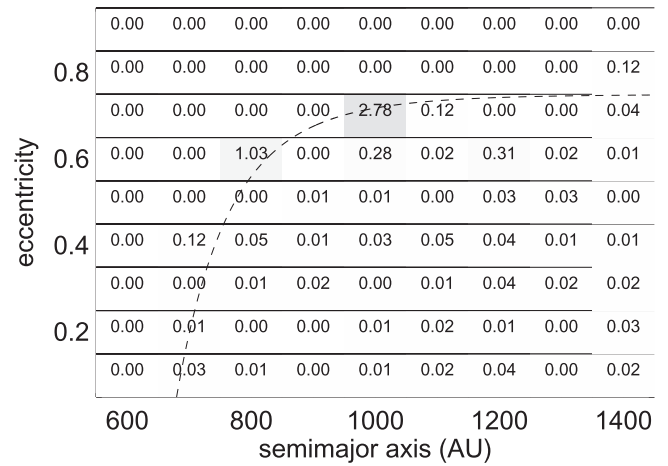


Figure 3. For a $20 M_e$ Planet Nine with $a_9 = [800, 1000]$ au and $e_9 = [0.6, 0.7]$ a marginal fit appears. At higher masses no simulations can reproduce the observations.

more qualitative than quantitative, as these simulations are exploratory and attempt to cover large ranges of phase space by including a limited number of particles per simulation and excluding three-dimensional effects. Nonetheless, the overall trends are clear. The lack of high perihelion objects between $100 < a < 200$ au strongly rules out all of the low semimajor axes and nearly all of the highest eccentricities, while the need to confine objects in perihelion longitude requires moderately high eccentricities or moderately low semimajor axes. The combined effect of these two constraints makes for a rather narrow combination of a_9 versus e_9 with acceptable solutions. In fact, the range is sufficiently narrow that it is clear that the grid spacing of our simulations is often too large to capture acceptable solutions at all semimajor axes or eccentricities.

Nonetheless, from the $10 M_e$ simulations we can discern the narrow range of acceptable results (Figure 2). In general, all simulations that cannot be excluded at the 99% confidence level fall with a range of $a_9 = [500, 800]$ au approximately along an empirically defined line of $e_9 = 0.75 - (450 \text{ au}/a_9)^8$, shown as the dashed line in Figure 2. Such orbits have a perihelion, q_9 , in the range $\sim [200, 340]$ au. The acceptable q_9 range is greater at smaller semimajor axis; at 600 au and beyond, all solutions have $q_9 \sim 200$ au.

For the $20 M_e$ simulations, the locus of acceptable a – e combinations shifts outward and can be fit with a similar empirical function $e_9 = 0.75 - (650 \text{ au}/a_9)^8$, but only from $a_9 = [800, 1000]$ au. Lower semimajor axes perturb the low semimajor axis KBOs to high perihelia, while higher semimajor axes fail to cluster the high semimajor axis KBOs appropriately. Higher-mass simulations cannot match the observations at all.

In Figure 4, we show, as an example, the Planet Nine–centered perihelion longitudes as a function of a of all objects that have $q < 80$ au and that have survived at least 3 Gyr, for the case of $M_9 = 10 M_e$, $a_9 = 500$ au, and $e_9 = 0.6$, one of the simulations along the acceptable locus. Objects anti-aligned with the planet have a longitude of 180° in this simulation, while those aligned will be at 0° longitude. This simulation shows the major effects that we have previously identified in the real data. Inside of 100 au little perturbation is visible. From 200 to 600 au the longitudes are confined around 180° , that is, they are anti-aligned with Planet Nine. And from 100 to 200 au

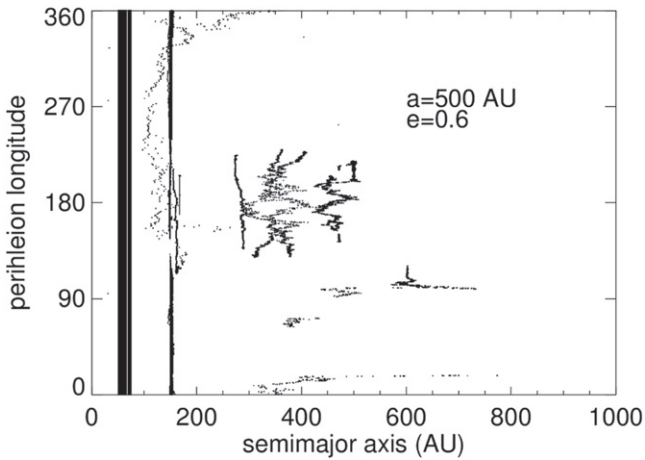


Figure 4. One of the successful simulations showing the orbital evolution of all objects with $q < 80$ au at times $t > 3$ Gyr. A collection of resonant stable high semimajor axis objects anti-aligned with Planet Nine (centered at Δ longitude of 180°) appears beyond 200 au, while from 100 to 200 au there is a slight preference for aligned orbits.

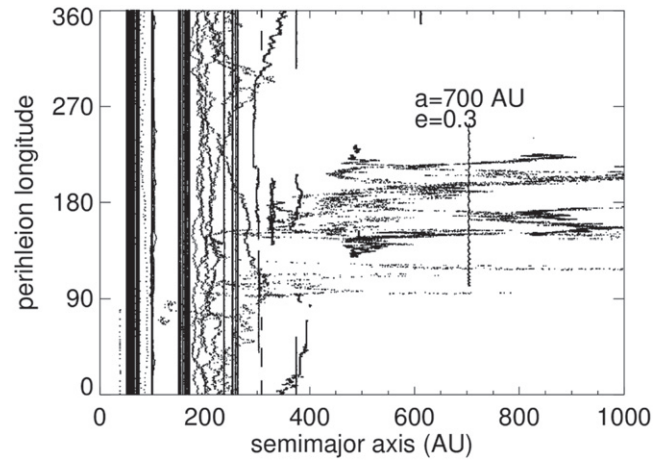


Figure 5. A low probability simulation. Clear anti-alignment does not develop until beyond 400 au, while aligned orbits appear only from approximately 300 to 400 au.

there is a slight tendency for a broad cluster centered on the longitude of the planet.

As a counter example, Figure 5 shows a simulation with $M_9 = 10M_e$, $a_9 = 700$ au, and $e_9 = 0.3$, which depicts many of the same general phenomena, but these phenomena do not develop until larger semimajor axes. For example, the anti-alignment does not begin until 400 au, while a broad aligned cluster can be seen from about 300 to 400 au. Even with the crudeness of these simulations, these basic effects are clear. The semimajor axis at which anti-alignment begins and the range where broad confinement is evident are strong indicators of the combination of semimajor axis and the eccentricity of Planet Nine.

3. CONSTRAINTS ON INCLINATION AND ARGUMENT OF PERIHELION

The planar simulations provide no constraints on inclination, i_9 , argument of perihelion ω_9 , or longitude of ascending node, Ω_9 , of Planet Nine. To examine the effects of these orbital elements on the Kuiper belt, we perform a second, fully three-dimensional suite of simulations. In these simulations we fix the semimajor axis and eccentricity to be 700 au and 0.6, respectively, values which are within our acceptable range of parameter space. The inclination dynamics are unlikely to be unique to the specific values of a_9 and e_9 , so we deem these simulations to be representative. We allow the inclination of Planet Nine to take values of $i_9 = 1, 10^\circ, 20^\circ, 30^\circ, 60^\circ, 90^\circ, 120^\circ$, and 150° .

Unlike the planar suite of calculations, here we start all planetesimals with their longitude of perihelia anti-aligned to that of Planet Nine. The starting values of planetesimals' longitudes of ascending node, on the other hand, are taken to be random. As demonstrated by Batygin & Brown (2016), dynamical sculpting of such a planetesimal population yields a configuration where long-term stable objects have longitudes of ascending node roughly equal to that of Planet Nine. In turn, this ties together ω_9 and Ω_9 through a fixed longitude of perihelion (which is the sum of these parameters).

Upon examination of these simulations, we find that efficiency of confinement of the distant population drops

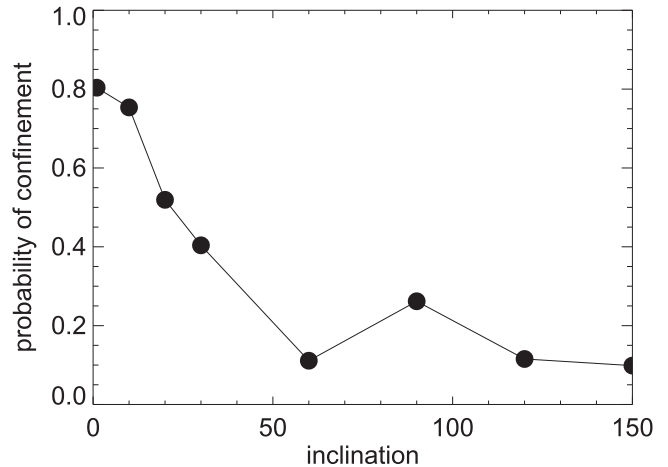


Figure 6. For simulations with $a_9 = 700$ au and $e_9 = .6$, the probability of confinement of seven randomly selected objects with $300 < a < 700$ and $q < 80$ au varies strongly with inclination of the planet.

dramatically with increased inclination of Planet Nine. To quantify this efficiency, we sample each simulation 1000 times, picking seven random objects from the sample of all objects in the range $a = [300, 700]$ au (as previously shown, these $a_9 = 700$ au simulations do not begin strong perihelion confinement until $a \sim 300$ au; as we are more interested in understanding the cluster than in specifically simulating our data at this point, we increase our semimajor axis range of interest). As before we restrict ourselves to time steps after 3 Gyr in which an object's orbit elements have $q < 80$ au, and we add the constraint that $i < 50^\circ$, to again account for observability biases. We calculate the fraction of times that the seven randomly selected objects are clustered within 94° (Figure 6). The confinement efficiency drops smoothly until, at an inclination of 60° and higher, it scatters around 20%. These results suggest, but do not demand, that Planet Nine has only a modest inclination.

One of the striking characteristics of the seven aligned distant KBOs is the large value of and tight confinement in the pole angle ($22^\circ \pm 6^\circ$; Figure 1). In examining the simulations that exhibit good confinement in longitude, we note that the polar angles of the simulated orbits are approximately

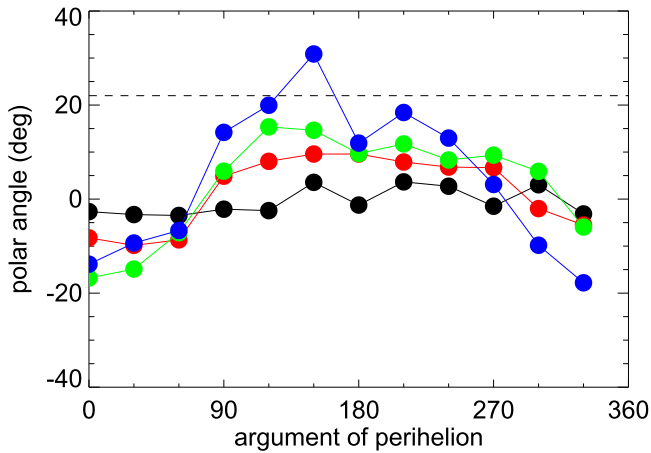


Figure 7. For the inclined simulations, the average polar angle of anti-aligned orbits varies systematically with ω_9 . The average polar angle of the seven most distant objects is 22° , shown as the dashed line. For simulations with high probability of confinement ($i_9 < 60^\circ$), the average polar angle only reaches values as high as 22° for $i_9 = 30^\circ$ and $\omega_9 = 150^\circ$. The black, red, green, and blue points correspond to the $i_9 = 1^\circ$, 10° , 20° , and 30° simulations, respectively.

perpendicular to the plane of Planet Nine, particularly for objects that come to perihelion in the plane of the planet. The implication of this phenomenon is that a pole angle of 22° suggests a minimum planet inclination of approximately 22° and an orbital plane (which is controlled by Ω_9) similar to the plane of the observed objects. To quantify this observation, we plot the median pole angle of our simulation objects that meet the criteria described above and that have perihelion latitudes between -25° and 0° like the real distant objects. We restrict ourselves to objects with perihelia south of the ecliptic both because the observed objects all have perihelia south of the ecliptic and also because we want to avoid any bias that would occur by a loss of observed objects north of the ecliptic due to the proximity of the galactic plane close to the perihelion positions. It is currently unclear whether the lack of clustered objects with perihelia north of the ecliptic is a dynamical effect or an observational bias. Figure 7 shows this mean polar angle as a function of argument of perihelion of Planet Nine. The maximum median polar angle occurs for $\omega_9 \sim 150^\circ$, a configuration where the plane of the planet passes through the perihelion positions of the objects, and that maximum is approximately equal to the inclination of the orbit, confirming our observation that the clustered objects are along the same orbit plane as the planet.

Based on the confinement probability and the large average pole angle of the real objects, we can infer that the inclination of Planet Nine is greater than $\sim 22^\circ$ and less than the inclination at which confinement becomes improbable, which, based on an interpolation of the data from Figure 5, occurs approximately around 40° . For inclinations of $\sim 22^\circ$, ω must be quite close to 150° . For inclinations of 30° , the allowable range for the argument of perihelion appears to be $\omega_9 \sim 120^\circ\text{--}160^\circ$.

While this analysis yields useful constraints, we quantify these results further by again sampling each of the simulations 1000 times and determining the probability of six randomly selected objects ($300 \text{ au} < a < 700 \text{ au}$, $q < 80 \text{ au}$, $i < 50^\circ$, survival time greater than 3 Gyr, and perihelion latitude between -25° and 0°) having perihelion longitudes clustered with 94° and having an average polar angle greater than 20°

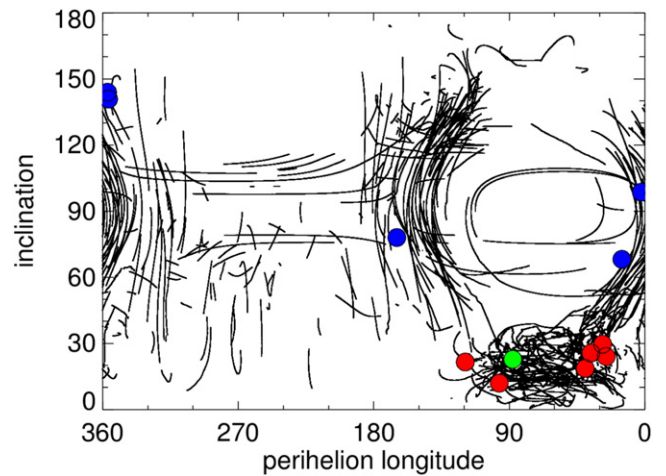


Figure 8. For simulations with $a_9 = 700 \text{ au}$, $e_9 = 0.6$, and $i_9 = 30 \text{ deg}$, examination of all objects with $300 < a < 700 \text{ au}$ and $q < 80 \text{ au}$ shows a low inclination population anti-aligned with Planet Nine and a high inclination population on either side of the anti-aligned population. The colored points are the same as in Figure 1(a), with the blue points showing that the highly inclined large semimajor axis Centaurs are closely aligned with the predicted high inclination locations.

with an rms spread of less than 6° . Almost all simulations can be ruled out at greater than the 99% confidence level. The only simulations that cannot be, unsurprisingly, those with an inclination of 30° and an argument of perihelion of 150° —which is the single best fit—and 120° and, additionally, a few other seemingly random combinations of $[i_9, \omega_9]$: $[90, 60]$, $[150, 0]$, $[150, 210]$, and $[150, 330]$, all in units of degrees. We examine all of these cases in detail below.

One strong prediction of the existence of a giant planet in the outer solar system is that it will cause Kozai-Lidov oscillations that will drive modest inclination objects onto high inclination perpendicular and even retrograde orbits and then back again. This effect can be seen, for example, in Figure 8, where we plot the evolution of perihelion longitude versus inclination for the simulations with 30° inclination (again, restricting ourselves to $300 > a > 700 \text{ au}$, $q < 80 \text{ au}$ and $t > 3 \text{ Gyr}$; note that the argument of perihelion of Planet Nine has no substantive effect on this plot, so we plot all arguments together). The five known objects in the outer solar system with $a > 200 \text{ au}$ and $i > 50 \text{ deg}$ are also shown. The simulations reproduce their perihelion longitudes and inclinations well, although they are all on the outer edge of the predicted clustering regions. An important caveat to note, however, is that the five high inclination objects are all Centaurs with $8 < q < 15 \text{ au}$. The high inclinations of these objects mean that they penetrate the giant-planet region much more easily and so can maintain their alignments much more easily than lower inclination Centaurs. Our simulations remove all objects inside 20 au , so we have not explored the dynamics interior to Uranus, but we note a systematic trend where objects with smaller perihelion distances move to the outer edge of the clustering regions, just like the real low perihelion objects appear to be. Clearly, simulations including all of the giant planets that allow us to study these high semimajor axis Centaurs are critical.

The perihelion locations of the perpendicular high semimajor axis Centaurs effectively rule out the possible higher inclination orbits for Planet Nine. The $i_9 = 90^\circ$ and $i_9 = 150^\circ$ cases do create high inclination objects, but their perihelia are sporadically distributed across the sky (Figure 9). We conclude

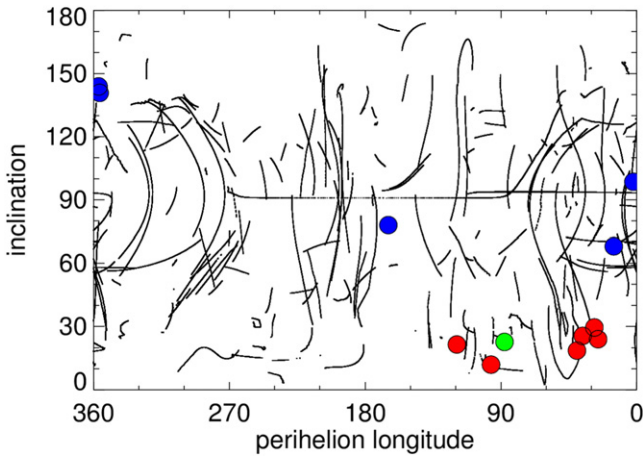


Figure 9. Simulations with $i_9 = 150^\circ$ produce little confinement of either the low or high inclination population.

that, of our simulated parameters, only the $i_9 = 30^\circ$, $\omega_9 = 150^\circ$ and $i_9 = 30^\circ$, $\omega_9 = 120^\circ$ are viable.

In order to complete our analysis in a tractable amount of time, each of the simulations used to explore parameter space above was limited in either dimensionality, number of particles, or in the range of starting parameter of the particles. In order to check that these limitations did not influence the overall results, we perform a final fully three-dimensional simulation with a large number of particles with randomly chosen starting angles. We choose to simulate Planet Nine with a mass of $10 M_e$, $a_9 = 700^\circ$, $e_9 = 0.6$, $i_9 = 30^\circ$, $\omega_9 = 0^\circ$, and $\Omega_9 = 0^\circ$ (note that the planet precesses over the 4 billion years of the integrations, but at this large semimajor axis the precession in ω_9 is only about 30° during the entire period, so we ignore this effect). These full simulations reproduce all of the relevant effects of the more limited simulations, giving confidence to our simulation results.

4. SKY POSITION

Based on comparison to our suite of simulations, we estimate that the orbital elements of Planet Nine are as follows. For 10 and $20 M_e$ planets, a_9 and e_9 are empirically defined in Section 2. We roughly bound these empirical functions with simple linear fits as a function of mass on the minimum and maximum semimajor axes of Planet Nine for the two masses and a simple linear fit to the empirical fitting function. We thus estimate that a_9 is in the range $[200 \text{ au} + 30M_9/M_e, 600 \text{ au} + 20M_9/M_e]$, where M_9 is approximately in the range $[5 M_e, 20 M_e]$, and that $e_9 = 0.75 - [(250 \text{ au} + 20M_9/M_e)/a_9]^8$.

The inclination is between approximately $22^\circ < i_9 < 40^\circ$, and the argument of perihelion is between $120^\circ < \omega_9 < 160^\circ$. We fix the perihelion longitude at $241^\circ \pm 15^\circ$. While these choices of parameter ranges have been justified in the analysis of the simulations above, they cannot be considered a statistically rigorous exploration of parameter space. Indeed, any attempt at such statistical rigor is not yet warranted: substantial uncertainty comes not just from the statistics of the objects themselves, but from the currently small number of simulations in the best-fit region of parameter space. Clearly, significantly more simulation is critical for a better assessment of the path of Planet Nine across the sky.

The last parameter we consider is the mass of Planet Nine, which we assume is in the range of $5\text{--}20 M_e$. To transform this

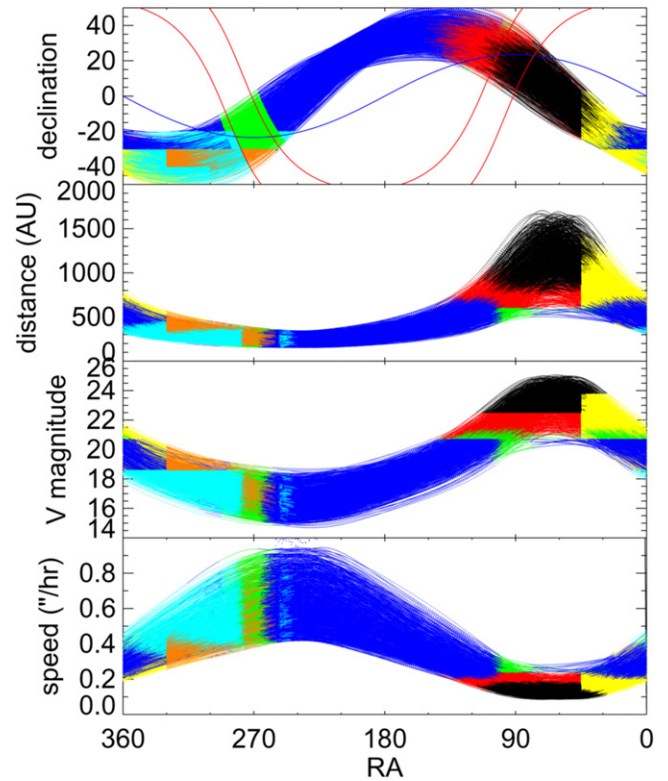


Figure 10. Using all constraints on the orbital and physical parameters of Planet Nine, we can predict the location, distance, brightness, and speed of the planet throughout its orbit. Regions within 10° of the galactic plane are outlined in red, and the ecliptic plane is shown in blue. The colored portions show regions where Planet Nine would have been or should be detected by previous or ongoing surveys. Light blue shows limits from the CRTS reanalysis, yellow shows Dark Energy Survey limits and coverage, dark blue shows Pan-STARRS transient analysis limits, green shows Pan-STARRS moving object analysis current limits, and red shows eventual Pan-STARRS expected limits. Orange shows the region exclusively ruled out by lack of observed perturbation to Saturn (Fienga et al. 2016; Holman & Payne 2016). The black regions show regions of phase space where Planet Nine could not have been or will not be detected in previous or currently planned surveys.

mass into an expected brightness requires assumptions of both radius (and thus composition) and albedo (and thus surface composition), neither of which is constrained by any of our observations. Fortney et al. (2016) consider a range of Planet Nine masses and core fractions. For masses between 5 and $15 M_e$ with 10% atmospheric mass fraction, the radius is approximately fit as $R_9 = [2.4 + 0.1(M_9/M_e)]R_e$, which we will use as our nominal relationship through this range and extending to $20 M_e$. In addition Fortney et al. (2016) find a quite high albedo value of 0.75 primarily due to Rayleigh scattering in the atmosphere. We assume, to be conservative, a range between 0.3, the approximate albedo of Neptune, and the modeled value of 0.75.

We now use our estimated orbital parameters to predict the orbital path of Planet Nine across the sky. We carry out a simple Monte Carlo analysis selecting uniformly across all of the parameter ranges. Figure 10 shows the sky location, heliocentric distance, magnitude, and sky motion at opposition for our suite of predicted orbits.

5. CURRENT OBSERVATIONAL CONSTRAINTS

While most wide-field surveys of the Kuiper belt have not been sensitive to sky motions smaller than about 1 arcsecond

per hour (i.e., Millis et al. 2002; Brown 2008; Petit et al. 2011), a few surveys have had the sensitivity and cadence to have potentially detected Planet Nine at some point in its orbit. We discuss all such surveys below.

5.1. WISE

The *WISE* spacecraft surveyed the entire sky twice in its 3.4 and 4.6 μm (W1 and W2) bands, allowing Luhman (2014) to rule out Saturn-sized planets—which have substantial enhanced short-wavelength emission owing to emission from internal heat—out to a distance of $\sim 30,000$ au. A $10 M_e$ planet, however, would not be expected to have this enhanced short-wavelength emission. For example, *ISO* detected nothing but reflected sunlight from Neptune from 2.5 to 5 μm (Burgdorf et al. 2003), with an average flux of about 5 mJy. The Luhman (2014) W1 limit corresponds to approximately 0.2 mJy, which suggests that Neptune itself could only be detected to ~ 70 au. As a confirmation, we examined the catalog of *WISE* single-source detections of Neptune itself. Neptune is detected 16 times with a signal-to-noise (S/N) of approximately 50 in the W1 band. Assuming that all of those images are coadded, Neptune could be detected with an S/N of 10 only to ~ 63 au, consistent with our estimate above. Fortney et al. (2016) suggest that the W1 brightness of Planet Nine could be enhanced above its blackbody level and thus potentially observable to a greater distance, but the sensitivity of the *WISE* data to Neptune-sized planets except at the closest possible distances remains low. The Luhman (2014) results thus provide no constraints on the position or existence of Planet Nine.

5.2. Catalina Real-time Transient Survey

While near-Earth object searches are performed at cadences poorly matched to the detection of objects in the outer solar system, they cover the sky multiple times in a year, allowing the possibility of detecting objects by their weekly or monthly motion. In Brown et al. (2015), we performed such an analysis from the Catalina Real-time Transient Survey (CRTS; Drake et al. 2009), which itself repurposed the Catalina Sky Survey near-Earth asteroid search into a transient survey. We collected all one-time transients over an eight-year period, that is, all instances in which an object was detected at a spot in the sky only once, and attempted to fit all combinations of four or more detections to Keplerian orbits. The Keplerian filter is strong. From $\sim 10^{19}$ potential combinations, we narrowed the detections down to eight known KBOs and zero false positives. Every bright KBO in the survey fields was detected, often dozens of times. The survey was determined to be essentially 100% complete to $V \sim 19.1$ in the north and $V \sim 18.6$ in the south. For some of the smaller potential values for semimajor axis and larger values of planetary radius, for example, Planet Nine would have been visible to this survey over a substantial portion of its orbit, though it was not detected.

5.3. The Pan-STARRS 1 Survey

The Pan-STARRS 1 telescope has surveyed large amounts of sky multiple times to moderate depths at decl. greater than -30° . We consider the analysis of the data in two stages.

The Pan-STARRS Survey for Transients. Like the earlier CRTS, the Pan-STARRS Survey for Transients (PST; Smartt et al. 2014) quickly disseminates detections of transients

sources detected in the sky. We have performed a similar analysis on the reported PST data, searching for viable Keplerian orbits. As of 2016 May 15, no series of transients can be found that fit an outer solar system body on any bound Keplerian orbit. Typical transient depths reached are $g = 21.0$, and based on the collection of reported transients, the survey appears to efficiently cover the sky north of -30 decl. and at galactic latitudes greater than about 10° . This survey rules out much of the sky within about 45° of the predicted perihelion point, with the exception of the region near the galactic plane.

The Pan-STARRS Outer Solar System Key Project. A survey for objects in the outer solar system was one of the initial goals of the Pan-STARRS survey. Holman et al. (2015) have now completed a preliminary analysis of the survey data and report no detections out to 600 au. While detailed sensitivity studies have yet to be completed, it is estimated that the survey is complete to approximately $r \sim 22.5$, though limits in the galactic plane are worse. An extended analysis is currently underway that will have the same brightness limits, but will remove the artificial restriction to objects closer than 600 au (M. J. Holman 2016, private communication). If these sensitivity estimates are correct, the Pan-STARRS 1 moving object survey has or will rule out a substantial fraction of the non-aphelion sky.

5.4. The Dark Energy Survey (DES)

The DES is performing the largest deep southern hemisphere survey to date. Some of the DES region covers the orbital path of Planet Nine (indeed one of the seven cluster objects, 2013 RF98, was detected in the DES). While cadences are not designed for ease of outer solar system detection, it is clear that the data will be sensitive to Planet Nine if it is in the survey area. The DES team estimates a Planet Nine detection limit of $r \sim 23.8$ (D. Gerdes 2016, private communication). The survey should be completed in 2018.

5.5. Additional Surveys

Additional surveys covering wide areas of the sky have been performed, but in all cases they are insensitive to the slow expected speeds of Planet Nine, they have too low of a survey efficiency to consider the region effectively surveyed, or they cover little or none of the region of the predicted orbital path. The large community surveys that are concentrating on specific areas of the sky, such as the VISTA surveys in the southern hemisphere and the Subaru Hyper-Suprime Cam survey along the celestial equator unfortunately do not overlap with the required search region.

In the future, the Large-Scale Synoptic Telescope is expected to survey much of the sky observable from its Chilean site to a single-visit depth of approximately $r \sim 24.5$ mag. The current survey strategy does not include visits to fields as far north as those at the extremes of the predicted Planet Nine orbital path, but if Planet Nine has not yet been found by the expected start of the LSST survey operations in 2023, a simple extension could quickly rule out nearly all but the faintest and most distant Planet Nine predictions.

At its most distant predicted locations, Planet Nine is faint and in the northern hemisphere. Subaru Hyper-Suprime Cam will be the instrument of choice for detecting the planet at these locations. We began a survey of these regions in the fall of

2015 and will attempt to cover all of this part of the predicted orbital path.

5.6. Additional Constraints

Fienga et al. (2016) perform full fits to the locations of all planets and nearly 300 asteroids observed from ancient times to the present with and without a $10 M_e$ Planet Nine at various positions along an orbit with $a_9 = 700$ au and $e_9 = 0.6$, consistent with the nominal orbit suggested in Batygin & Brown (2016). They find that the strongest constraint on the existence of Planet Nine comes from the very precise measurements of the distance to Saturn as measured by the *Cassini* spacecraft over the past decade. With no Planet Nine, their best fit to the position of Saturn has Earth–Saturn distance residuals that roughly follow a sinusoid with a 12-year period and a full amplitude of ~ 70 m. Previous fits to the ephemeris of Saturn using the identical data, however, found smaller residuals and no evidence of systematic variation (Hees et al. 2014), while even more recent fits, leading to the creation of the DE435 JPL planetary ephemeris, put even tighter constraints on any remaining residuals. It thus remains unclear whether any residual is present in the Earth–Saturn distance. We remain agnostic about the existence of residuals in the distance to Saturn, but instead assume that the signal apparently detected by Fienga et al. (2016) is at or near the level of the systematic errors in this type of analysis and that larger signals from Planet Nine could be detected. At its the nearest possible locations, in particular, Planet Nine would cause such a large effect on the Earth–Saturn distance that the Fienga et al. (2016) analysis and an extension by Holman & Payne (2016) (which assumes the same residuals) can rule out any of the Planet Nine solutions near perihelion over the range of R.A. of R.A.₉ > 255, R.A.₉ < 2 deg.

A recent paper (Malhotra et al. 2016) makes no attempt to explain spatial alignments, but instead attempts to simplistically look for mean-motion commensurabilities in the distant KBOs, in hopes of being able to constrain both a_9 and the location of Planet Nine within its orbit. Specifically, they assume that the four most distant KBOs are in N:1 and N:2 resonances and examine the implications for Planet Nine. Such an approach could, in principle, work in the circular restricted three-body problem, but, as shown in Batygin & Brown (2016), highly elliptical orbits are required to explain the spatial confinement of the orbits, and no specific resonances dominate the disturbing function in this elliptical problem. Indeed, no particular preference for type of critical angle or even resonance order can be identified in the dynamical simulations shown here. Rather, the crossing orbits evolve chaotically but maintain long-term stability by residing on a interconnected web of phase-protected mean-motion resonances. The assumption of simple low-order resonance is thus unlikely to be justified. Not surprisingly, the Planet Nine orbits produced by these assumptions do not produce the spatial confinements of the KBOs that are observed. Thus, it appears that no useful constraint on the orbit or position can be drawn from this method.

5.7. Joint Constraints

In Figure 10, we show the regions of the potential orbits of Planet Nine that have been ruled out by the above constraints (or, in the case of the ongoing DES and final Pan-STARRS analysis, where the planet might still be found by these

surveys). The existence of Planet Nine can be ruled out over about two-thirds of its orbit. The vast majority of the orbital region in which Planet Nine could be located is beyond about 700 au and within about 60° of its aphelion position. For the eccentric orbits considered here, Planet Nine spends greater than half of its time at these distances, so finding it currently at these locations near aphelion would be expected. At its most distant allowed location and with a Neptune-like albedo, a $20 R_e$ Planet Nine is approximately $V = 25$. While faint, such an object would be well within the limits of 10 m class telescopes.

6. CONCLUSIONS

The existence of a distant massive perturber in the outer solar system—Planet Nine—explains several hitherto unconnected observations about the outer solar system, including the orbital alignment of the most distant KBOs, the existence and alignment of high perihelion objects like Sedna, and the presence of perpendicular high semimajor axis Centaurs. These specific observations have been compared to suites of numerical integrations in order to constrain possible parameters of Planet Nine. The current constraints must be considered preliminary: our orbital simulations needed to cover substantial regions of potential phase space, and so were, of necessity, sparsely populated. At present, the statistical reliability of our constraints are limited as much by the limited survey nature of the simulations as by the small number of observed objects themselves. Continued simulation could substantially narrow the potential search area required. In addition, continued simulation is required in order to understand one effect not captured in the current models: the apparent alignment of the argument of perihelion of the 16 KBOs with the largest semimajor axes (Trujillo & Sheppard 2014). Some of this apparent alignment may come from yet unmodeled observational biases related to the close proximity of the perihelion positions of the most distant objects to the galactic plane, while some may be a true as-yet-unmodeled dynamical effect.

As important as continued simulation, continued detection of distant solar system objects is the key to refining the orbital parameters of Planet Nine. Each addition KBO (or Centaur) with $a > 100$ au tightens the observational constraints on the location of Planet Nine (or, alternatively, if significant numbers of objects are found outside of the expected cluster location, the objects can refute the presence of a Planet Nine).

Interestingly, the detection of more high semimajor axis perpendicular objects (whether Centaurs or KBOs) has the possibility of placing the strongest constraints in the near term. While we have currently only used the *existence* of these objects as a constraint, their perihelion locations and values of ω change strongly with ω_9 and i_9 and so can be used to better refine these estimates. Though there are only currently five known of these objects, they are being discovered at a faster rate than the distant KBOs, so we have hope of more discoveries soon. As with the distant KBOs, of course, detection of these objects also has the strong possibility of entirely ruling out the existence of Planet Nine if they are not found with perihelia in the locations predicted by the hypothesis.

REFERENCES

- Batygin, K., & Brown, M. E. 2016, *AJ*, 151, 22
 Brasser, R., Duncan, M. J., & Levison, H. F. 2006, *Icar*, 184, 59

- Brown, M. E. 2008, in *The Solar System Beyond Neptune*, ed. M. A. Barucci et al. (Tucson, AZ: Univ. Arizona Press), 335
- Brown, M. E., Bannister, M. T., Schmidt, B. P., et al. 2015, *AJ*, **149**, 69
- Brown, M. E., Trujillo, C., & Rabinowitz, D. 2004, *ApJ*, **617**, 645
- Burgdorf, M., Orton, G. S., Davis, G. R., et al. 2003, *Icar*, **164**, 244
- Chambers, J. E. 1999, *MNRAS*, **304**, 793
- Chen, Y.-T., Kavelaars, J. J., Gwyn, S., et al. 2013, *ApJL*, **775**, L8
- Drake, A. J., Djorgovski, S. G., Mahabal, A., et al. 2009, *ApJ*, **696**, 870
- Dukes, D., & Krumholz, M. R. 2012, *ApJ*, **754**, 56
- Fienga, A., Laskar, J., Manche, H., & Gastineau, M. 2016, *A&A*, **587**, L8
- Fortney, J. J., Marley, M. S., Laughlin, G., et al. 2016, *ApJL*, in press (arXiv:1604.07424)
- Gladman, B., & Chan, C. 2006, *ApJL*, **643**, L135
- Gomes, R. S., Matese, J. J., & Lissauer, J. J. 2006, *Icar*, **184**, 589
- Gomes, R. S., Soares, J. S., & Brasser, R. 2015, *Icar*, **258**, 37
- Hees, A., Folkner, W. M., Jacobson, R. A., & Park, R. S. 2014, *PhRvD*, **89**, 102002
- Holman, M. J., Chen, Y.-T., Lin, H.-W., et al. 2015, *BAAS*, **47**, 211.12
- Holman, M. J., & Payne, M. J. 2016, arXiv:1604.03180
- Kenyon, S. J., & Bromley, B. C. 2004, *Natur*, **432**, 598
- Luhman, K. L. 2014, *ApJ*, **781**, 4
- Malhotra, R., Volk, K., & Wang, X. 2016, *ApJL*, **824**, L22
- Millis, R. L., Buie, M. W., Wasserman, L. H., et al. 2002, *AJ*, **123**, 2083
- Morbidelli, A., & Levison, H. F. 2004, *AJ*, **128**, 2564
- Petit, J.-M., Kavelaars, J. J., Gladman, B. J., et al. 2011, *AJ*, **142**, 131
- Rickman, H., Froeschlé, C., Froeschlé, C., & Valsecchi, G. B. 2004, *A&A*, **428**, 673
- Smartt, S. J., Smith, K. W., Wright, D., et al. 2014, *ATel*, **5850**
- Trujillo, C. A., & Sheppard, S. S. 2014, *Natur*, **507**, 471